



THE UNIVERSITY *of* EDINBURGH

Edinburgh Research Explorer

## Fastblade: A Technological Facility for Full-Scale Tidal Blade Fatigue Testing

**Citation for published version:**

Lopez Dubon, S, Vogel, CR, Garcia Cava, D, Cuthill, F, McCarthy, E & Ó Brádaigh, CM 2023 'Fastblade: A Technological Facility for Full-Scale Tidal Blade Fatigue Testing' Social Science Research Network (SSRN). <https://doi.org/10.2139/ssrn.4400928>

**Digital Object Identifier (DOI):**

[10.2139/ssrn.4400928](https://doi.org/10.2139/ssrn.4400928)

**Link:**

[Link to publication record in Edinburgh Research Explorer](#)

**Document Version:**

Early version, also known as pre-print

**General rights**

Copyright for the publications made accessible via the Edinburgh Research Explorer is retained by the author(s) and / or other copyright owners and it is a condition of accessing these publications that users recognise and abide by the legal requirements associated with these rights.

**Take down policy**

The University of Edinburgh has made every reasonable effort to ensure that Edinburgh Research Explorer content complies with UK legislation. If you believe that the public display of this file breaches copyright please contact [openaccess@ed.ac.uk](mailto:openaccess@ed.ac.uk) providing details, and we will remove access to the work immediately and investigate your claim.



# **FASTBLADE: A TECHNOLOGICAL FACILITY FOR FULL-SCALE TIDAL BLADE FATIGUE TESTING**

Sergio. Lopez Dubon<sup>1\*</sup>, Christopher. Vogel<sup>2</sup>, David. Garcia Cava<sup>1</sup>, Fergus. Cuthill<sup>1</sup>, Edward D. McCarthy<sup>1</sup>, Conchur M. Ó Bradaigh<sup>1</sup>

<sup>1</sup> School of Engineering, The University of Edinburgh  
Edinburgh, Scotland/The United Kingdom

<sup>2</sup> Department of Engineering Science, University of Oxford  
Oxford, England/The United Kingdom

\*Corresponding author

Email address: Sergio.LDubon@ed.ac.uk (Sergio Lopez Dubon)

# FASTBLADE: A TECHNOLOGICAL FACILITY FOR FULL-SCALE TIDAL BLADE FATIGUE TESTING

Sergio. Lopez Dubon<sup>1\*</sup>, Christopher. Vogel<sup>2</sup>, David. Garcia Cava<sup>1</sup>, Fergus. Cuthill<sup>1</sup>, Edward D. McCarthy<sup>1</sup>, Conchur M. Ó Bradaigh<sup>1</sup>

<sup>1</sup> School of Engineering, The University of Edinburgh  
Edinburgh, Scotland/The United Kingdom

<sup>2</sup> Department of Engineering Science, University of Oxford  
Oxford, England/The United Kingdom

## ABSTRACT

Fatigue testing of tidal turbine blades requires the application of cyclic loads without the ability to match the natural frequency of the blade due to their high stiffness and the associated thermal issues of testing composite materials at those frequencies (i.e., 18-20 Hz). To solve this, loading the blades with an auxiliary system is necessary; in most cases, a conventional hydraulic system tends to be highly energy demanding and inefficient. A regenerative digital displacement hydraulic pump system was employed in the FastBlade fatigue testing facility, which saved up to 75% compared to a standard hydraulic system. A series of equivalent target loads were defined using Reynolds-Averaged Navier Stokes (RANS) simulations (based on on-site collected water velocity data) and utilised in FastBlade to demonstrate an efficient way to perform fatigue testing. During the test, a series of measurements were performed on the blade response and the Fastblade test structure itself, providing novel insights into the mechanical behaviour of a blade, and enabling improved testing practice for FastBlade. The blade withstood 20 years (equivalent) of accelerated fatigue loading without catastrophic failure. This test data will enable FastBlade to identify improvements to the testing procedures, i.e., control strategies, load introduction, instrumentation layout, instrument calibration, and test design.

Keywords: Testing, Fatigue, Tidal Steam Blades, Composites

\* Corresponding author: [Sergio.LDubon@ed.ac.uk](mailto:Sergio.LDubon@ed.ac.uk)

## 1. INTRODUCTION

### 1.1 Tidal Energy Sector and Current Scenario for Tidal Turbine Blade Design

It is projected that tidal and wave sources could contribute 100GW to the EU power grid by 2050, powering a third of homes and adding €140 bn of economic activity and ca. 500,000 jobs in Europe alone [1]. Globally, 150-800 TWh (terawatt hours) or EUR 40 billion per year of activity is projected [2]. Tidal stream energy is a key sector contributing to this growth, and horizontal axis turbines (HATs) are the underpinning technology. Much of the supporting technology and design methodology for HATs have been adapted from the wind turbine sector. However, it has not been possible to map designs and design methodology for wind turbine blades directly to tidal turbine blades, however, as the latter operates in a medium (seawater) that is 800 times denser than air.

38 Thus, the loads handled are significantly higher and more problematic to manage. Preliminary  
39 design of tidal turbine blades based on blade element momentum theory and simplified Finite  
40 Element Models of composite blades are given for static loading in [3] and for design life  
41 calculations in [4,5].

42 Tidal turbine blades are much shorter than the largest offshore wind blades (e.g., 6-8 m v. 100 m  
43 plus), since they operate in a medium ca. 800 times denser. Secondly, to manage the higher fluid  
44 stresses, they can have blade root sections with wall thickness ca. 100 mm, compared with tip  
45 thicknesses ca. 6-10 mm [6]. This means that the transition from the blade root to tip occurs rapidly  
46 over the length of the blade, which tends to create particular stress concentrations over a narrow  
47 root-to-body transition zone. These high-stress concentrations, in turn, create an elevated risk of  
48 fatigue failure over the 20-year design life of a typical blade.

49 Currently, there are insufficient data and understanding of fatigue in tidal blades, which is one of  
50 the reasons that tidal stream energy retains a relatively high levelised cost of energy (LCOE)  
51 compared with other renewable energy technologies. Cost of energy is expected to fall as more  
52 tidal turbines are built with significant learning and innovations to follow, in a similar fashion to  
53 offshore wind. In 2022, four tidal companies were awarded UK Contracts for Difference of  
54 £178/MWh, which is high compared to the current LCOE of £37.35/MWh for offshore wind  
55 projects [7]. This has led to a renewed focus on improved test methods, more representative data,  
56 and a new design methodology to radically reduce turbine blade fatigue failure risk.

57 In recent years, several advances have been made in full-scale fatigue testing of composite material  
58 tidal blades. These include the test performed in 2018 by [8] in the Large Structure Laboratory of  
59 the University of Galway, where a 3/8<sup>th</sup> scaled-down blade design by OpenHydro was tested. The  
60 test was performed using a servo-hydraulic actuator system, achieving a maximum load amplitude  
61 of 35kN and 275,000 cycles.

62 Later, in 2020, a new turbine blade fatigue test standard was published, IEC TS 62600-3:2020 [9],  
63 which codifies a test method for fatigue testing of full-scale tidal blades, and in 2022, the new  
64 FastBlade facility at Port of Rosyth, Scotland, was opened, which has the capability to deliver  
65 accelerated lifetime fatigue testing of a full-scale tidal blade and other long slender structures [10].  
66 These two developments enabled this Supergen ORE Hub LoadTide project, the first project to  
67 achieve accelerated lifetime fatigue testing of a tidal turbine blade.

68 Also in 2022, at the University of Galway, another fatigue test was performed [11] with two  
69 full-scale blades of 2 and 3 meters in length from SCHOTTEL HYDRO. The test campaign  
70 consisted of natural frequency, static, fatigue and residual strength testing. For the fatigue test of  
71 the 2-meter blade, a maximum load of 6.9 kN was achieved during 150,000 cycles at 0.3Hz; and  
72 for the 3-meter blade, a maximum load of 14 kN was reached during 16,000 cycles at 0.1Hz.

73 In this paper, we show how FastBlade is the first test facility globally capable of delivering a high  
74 load during high cycle fatigue testing of a tidal blade, performing 31,775 cycles at 1 Hz with a  
75 target load of 183.7 kN, making such a test economic for the first time. The facility is enabled by  
76 a unique pumping system that features regenerative pumping and digital displacement hydraulics  
77 [12–14]. The combination of these features can reduce effective testing energy by up to 75%, thus

78 enabling testing to be delivered in several weeks rather than months; this renders such testing  
79 economic for blade developers. This paper describes the first tidal turbine blade test conducted in  
80 FastBlade in the Summer of 2022, which generated fatigue performance data for a previously  
81 deployed tidal turbine blade installed on a tidal stream turbine at Fall of Warness, Orkney,  
82 Scotland, UK.

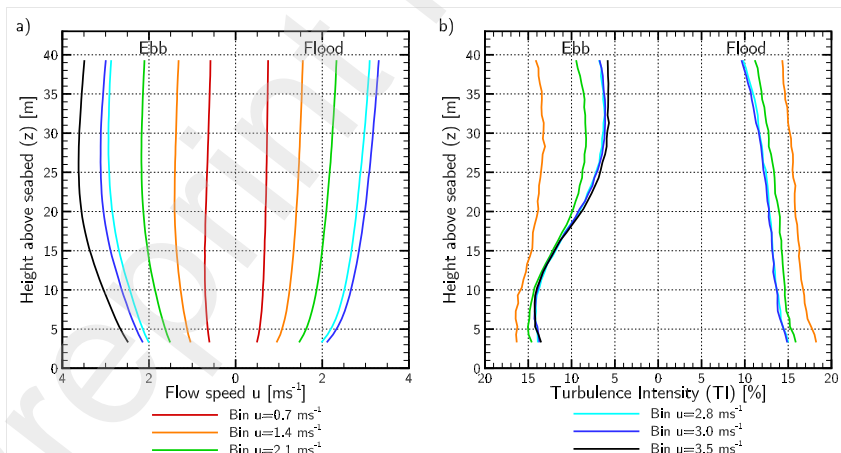
## 83 2. METHODS

### 84 2.1 Site Data

85 The flow data used in this project were sourced from the ReDAPT project at the Fall of Warness,  
86 European Marine Energy Centre (EMEC), Orkney UK [15–17]. The data was collected using two  
87 acoustic Doppler current profilers deployed between 19 July and 2 August 2013. The profilers  
88 were positioned 0.8 m above the seabed and sampled the flow at a frequency of 0.5 Hz. The mean  
89 operating depth of the profilers during deployment was 43.2 m and 46.2 m due to the slightly  
90 different seabed conditions at their respective locations.

91 Flow speed and turbulence intensity data were binned into hub-height mean flow speed bins of  $U_\infty$   
92 = (0.7, 1.4, 2.1, 2.8, 3.0, 3.5)  $\text{m s}^{-1}$  for both the flood and ebb tides, noting that  $U_\infty = 3.5 \text{ m s}^{-1}$   
93 was only achieved during the ebb tide. Data was only included if the wave height was less than 1  
94 meter. The ensemble length for all statistics was 5 minutes, and a  $0.12 \text{ cm s}^{-1}$  noise correction  
95 estimate was made to the turbulence intensity data following [16].

96 Vertical profiles of flow speed and turbulence intensity are presented in Figure 1, demonstrating  
97 the differences in the simulated profiles between the ebb and flood tides. A slight reduction in flow  
98 speed near the surface during the ebb tides arises because the flow is funnelled around the islands  
99 surrounding the Falls of Warness site. A consequence of this is that the fastest flows were  
100 encountered about halfway through the water column at the highest flow speed bins. This also  
101 gives rise to the differences in the turbulence intensity profiles between the flood and ebb tides.  
102 Consequently, the standard deviation of the flow speed across the rotor plane is consistently higher  
103 for flood tides than the ebb tides for a specified hub-height flow speed, as shown in [16].



104

105 *Figure 1. Simulated vertical profiles of (a) flow speed (u) and (b) turbulence intensity (TI) at the Fall of Warness ReDAPT site,*  
106 *based on [16]. Data binned by hub-height mean velocity for ebb and flood tide conditions. The turbine hub height is 19 m.*

107 During the flood tide, the velocity profiles follow an approximately 1/6<sup>th</sup> power law, whereas this  
108 is closer to a 1/5<sup>th</sup> power law for the ebb tide in the lower portion of the flow, which is unaffected  
109 by the near-surface flow speed reduction present in the Falls of Warness described above.

110 *Table 1. Standard deviation in simulated flow speed across the rotor plane in flood and ebb tides as a function of hub-height flow*  
111 *speed.*

Flow speed bin [m s <sup>-1</sup> ]	Ebb tide	Flood tide
0.7	0.0429	0.0639
1.4	0.0944	0.1546
2.1	0.1889	0.2257
2.8	0.2782	0.2866
3.0	0.2833	0.3123
3.5	0.3331	-

## 112 2.2 Computational Model

113 A suite of unsteady Reynolds-Averaged Navier Stokes (URANS) simulations were performed  
114 using the computational fluid dynamics (CFD) solver OpenFOAM (version 2.3.1). The choice of  
115 URANS simulation draws on the work of Ahmed et al., which found that URANS and Large Eddy  
116 Simulation predict very similar phase-averaged loads and blade pressure distributions in low onset  
117 turbulence flows [18], as is the focus of this paper. The simulations were performed using the  
118 PimpleFoam PISO algorithm, and turbulence closure was provided by the  $k - \omega$  SST model with  
119 the 2003 updated coefficients [19]. The simulated time for each case was 400s, with a time step of  
120 0.03s.

### 121 2.2.1 Computational Domain

122 The computational domain was 250 m long, 520 m wide and 43 m tall, corresponding to the height  
123 of the ReDAPT site. The domain width was set to achieve a small geometric blockage ratio (ratio  
124 of rotor swept area to channel cross-sectional area) of 1.14%. A vertical flow profile was imposed  
125 at the inlet of the computational domain using the atmospheric boundary layer inlet condition  
126 available in OpenFOAM. A no-slip wall boundary condition at the bottom of the domain and a  
127 stress boundary condition at the top sustained the flow profile. At the outlet boundary, the static  
128 pressure was set to a fixed value of 0 Pa, and zero gradient boundary conditions were applied to  
129 the turbulence and velocity scalars. Symmetry conditions were applied to the lateral boundaries of  
130 the domain. The inflow and top boundary conditions were adjusted to match the flow profile  
131 observed from the ReDAPT data [15].

### 132 2.2.2 Meshing Strategy

133 The domain was discretised with an Octree mesh to allow a concentration of mesh resolution near  
134 the rotor region. The mesh parameters' convergence was evaluated by comparing the simulated

135 flow profile to the field observations and the spanwise distribution of blade forces. A spatially  
136 homogeneous grid dimension of 1.5 m was found to capture well the velocity gradients near the  
137 seabed and surface boundaries and provide good agreement with field observations of the mean  
138 velocity profile.

139 Two additional levels of grid refinement were employed near the rotor and in the wake region. An  
140 intermediate level of resolution of 0.75 m was employed in a region  $-0.73d \leq x \leq 1.77d$ ,  
141  $-0.94d \leq y \leq 0.94d$  and  $-1d \leq z \leq 0.61d$  around the centre of the rotor, where  $x$  is the  
142 streamwise coordinate,  $y$  is the cross-stream coordinate, and  $z$  is the vertical coordinate. The rotor  
143 region was further refined with a homogeneous dimension of 0.1875 m in a region  
144  $-0.18d \leq x \leq 1.44d$ ,  $-0.67d \leq y \leq 0.67d$ ,  $-0.67d \leq z \leq 0.61d$ . The final mesh contained  
145 approximately  $2.8 \times 10^6$  elements.

146 The actuator line method represents the turbine blades (detailed below). The actuator lines are  
147 swept through the static mesh. Thus, no rotating sub-domains or mesh interfaces are required, as  
148 would be typical for blade-resolved models. This represents a significant saving in computational  
149 cost. However, as described above, it should be noted that the mesh is refined close to the turbine  
150 to resolve the large velocity gradients around the blades.

### 151 **2.2.3 Actuator Line Model**

152 The turbine was represented using the actuator line method of Sørensen & Shen [20] implemented  
153 in OpenFOAM as a user-defined shared object library. The actuator line model represents the rotor  
154 blades with rotating lines along which force is applied to the flow. Each line corresponds to a  
155 blade. The actuator forces, therefore, represent an additional term in the momentum equations. The  
156 in-house model has been extensively validated against a number of reference turbines; see, for  
157 example, [21,22].

158 The blade forces are calculated using 2D blade element theory at 100 collocation points distributed  
159 sinusoidally along the blade length in order to capture the changes in forces in the root and tip  
160 regions of the blades. The lift and drag data that were employed are described in Section 2.3. The  
161 flow field around each blade was sampled using the potential flow equivalence method proposed  
162 by [21], and reimposed on the flow using the Gaussian smearing technique of Sørensen & Shen  
163 [20]. The calculated blade forces were modified by the tip loss model of Shen et al. [23] to account  
164 for the 3D flow effects that reduce the blade forces near the tips.

165 The turbine nacelle, radius  $R_{\text{hub}} = 1.35$  m, was represented using a cell-blocking method following  
166 [24]. This method blocks fluxes into cells by applying a sufficiently large body force to the selected  
167 cells, thus enforcing the velocity to be zero, allowing impermeable bodies to be represented in the  
168 numerical domain without requiring the geometry to be resolved explicitly.

## 169 **2.3 Blade data**

### 170 **2.3.1 General information**

171 The blade is part of the DeepGen tidal project and was designed by Tidal Generation Limited  
172 (TGL) and manufactured by Aviation Enterprises Limited. The final blade design report was

173 issued in 2008, and the company responsible for the blade design no longer exists. The rights were  
174 bought by another company (Airborne), but some design documents were lost and not provided to  
175 FastBlade before testing. The blade was taken from the decommissioned 500kW tidal stream  
176 turbine, previously installed at EMEC's grid-connected test site at the Fall of Warness.

### 177 **2.3.2 Geometry**

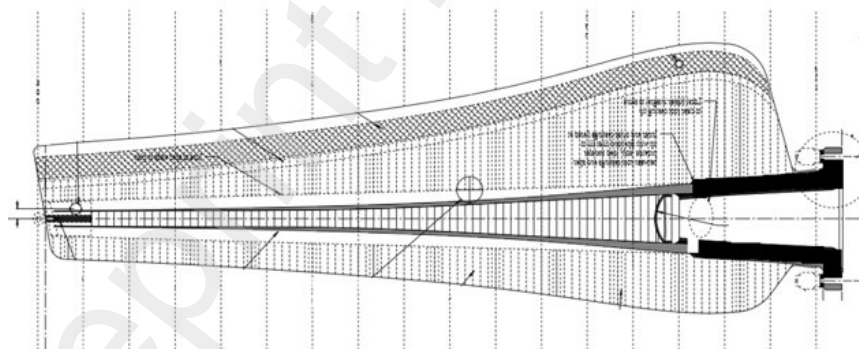
178 The blade cross-section is defined by the NACA 63-4XX aerofoil series, with XX representing the  
179 section thickness-to-chord ratio. The thickness-to-chord ratio decreased from 55% near the blade  
180 root to a minimum of 18% at the tip. The innermost portion of the blade was taken to have a  
181 cylindrical cross-section with an implied thickness-to-chord ratio of 100%.

182 NACA aerofoil coordinates were determined following [25], with the geometry sampled at 300  
183 equally-spaced points. Aerofoil lift and drag characteristics as a function of angle of attack  $\alpha$  were  
184 computed using QBlade with the chord-based Reynolds number in the range  $10E6 < Re < 18E6$   
185 The critical number  $N_{crit} = 9$  for all cases.

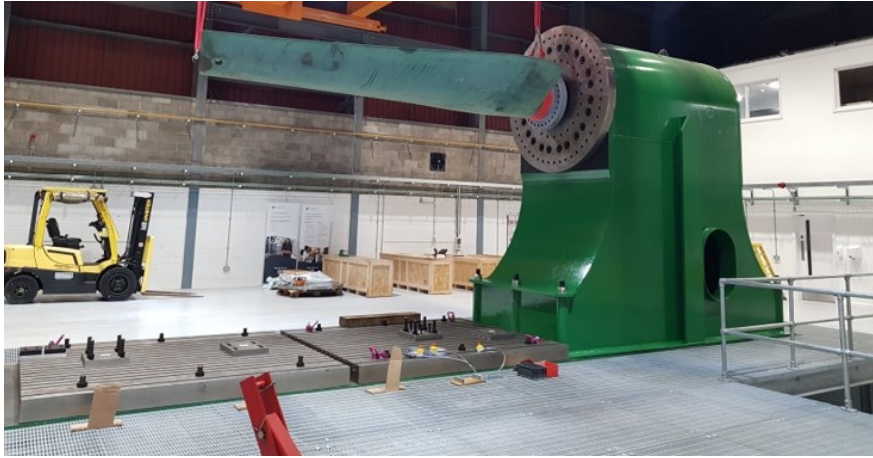
### 186 **2.3.3 Structure**

187 The entire blade is covered with an 8mm thick glass fibre skin manufactured using  $\pm 45^\circ$   
188 unidirectional glass fibre prepreg. The dashed lines in **Error! Reference source not found.**  
189 perpendicular to the blade span represent the locations of pairs of 3 mm thick glass fibre ribs used  
190 to stiffen the blade. They allow pressure transfer from the blade skins to the spar caps and are  
191 manufactured using  $\pm 45^\circ$  glass fibre unidirectional prepreg. The spar cap is manufactured using  
192 80% unidirectional carbon fibre epoxy prepreg, with the remaining 20% containing  $90^\circ$  fibres to  
193 improve the transverse strength and stiffness of the spar region. The shear webs are designed to  
194 resist the blade's flapwise shear loads and torsional bending and are manufactured using  $\pm 45^\circ$   
195 carbon fibre epoxy prepreg. Finally, a rear glass fibre epoxy spar connects the suction and pressure  
196 sides 100mm away from the trailing edge to relieve the trailing edge joint from peel stresses [26].

197







199

200 *Figure 2. Technical Drawing of the Test Blade Looking from the Top View [26] and the original blade.*

201

### 3. EXPERIMENTATION

202 Once the loads were defined, the mechanical test campaign followed the IEC TS 62600-3:2020  
 203 standard, performed in the following test sequence: 1<sup>st</sup>, total mass and centre of gravity; 2<sup>nd</sup>, natural  
 204 frequency (3 repeats); 3<sup>rd</sup>, static test; 4<sup>th</sup>, natural frequency (3 repeats); 5<sup>th</sup>, fatigue test; 6<sup>th</sup>, natural  
 205 frequency test (3 repeats); 7<sup>th</sup>, static test; 8<sup>th</sup>, natural frequency (3 repeats).

#### 206 3.1 FastBlade Facility Description

207 FastBlade features a 70-tonne reaction frame capable of resist high loads during static and fatigue  
 208 testing (see Table 2.), combined with 880 litres per minute of reversible hydraulic flow.

209 *Table 2. Strong Wall Load Capacities.*

Load Capacity	Moment (MN-m)	Shear (MN)
FATIGUE (Up to 400 million cycles pushing)	4.70	0.94
FATIGUE (Up to 400 million cycles Pulling)	4.70	0.94
STATIC (Assuming quasi-static loading Pulling)	11.96	2.39
STATIC (Assuming quasi-static loading Pushing)	10.74	2.13

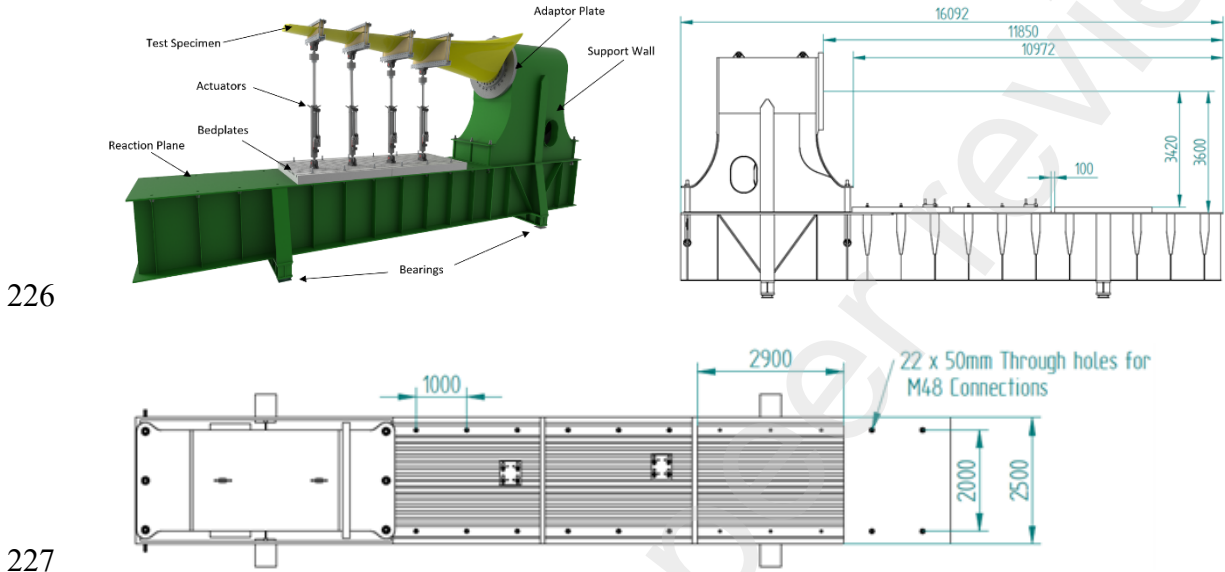
##### 210 3.1.1 FastBlade Frame

211 The reaction frame supports all test specimens and loads (see Figure 3). It consists of a reaction  
 212 plane, support wall, T-Slot bed plates and adapter plate, all mounted-on bridge bearings. The  
 213 reaction frame is in a pit in the floor (2.5 m deep) with the top surface of the reaction plane level  
 214 with the foundation of the building.

##### 215 3.1.2 FastBlade Hydraulic system

216 FastBlade employs 4 Digital Displacement hydraulic reverse pumps developed by Danfoss (see  
 217 Figure 4). The ability of the pumps to work in reverse flow flux allows them to recover the energy

218 used during the test. First, an amount of energy is used to apply a load to the specimen producing  
 219 a deformation of the same. Once the target load is achieved, no more power is added to the system.  
 220 The pumps then run in reverse, now powered by the weight and spring-back of the specimen,  
 221 generating energy that can be used to power the pump motor in the next cycle. This system allows  
 222 FastBlade to operate with up to 80% less energy used than similar-sized hydraulic systems.  
 223 Moreover, the pumps also provide all the control of the actuators, meaning that we can avoid the  
 224 cost of expensive servo hydraulics and operate with relatively simple actuators, allowing the  
 225 implementation of compound loads that can better represent complex ocean interactions.



226  
 227  
 228  
 229

Figure 3. Reaction frame general arrangement (Top right-hand reaction frame with the specimen, top left-hand lateral section, bottom horizontal section).



230  
 231 Figure 4. . FastBlade's Digital Displacement hydraulic pumps.

232 **3.1.3 Data Collection**

233 For this test campaign, we collected data from both the blade specimen and the FastBlade system.  
 234 All sensors were calibrated before the experimental campaign, the appropriate sensors were  
 235 zeroed, and reference measures ("zero readings") were taken before each test. The data acquisition  
 236 system used a 4x NI cDAQ 9189 chassis synchronised using a time-sensitive network to provide  
 237 a reliable distributed logging system. Various C-Series modules are used with the chassis for

238 logging the different signal types. All the data logging is controlled via Flexlogger software, which  
 239 allows the visualisation and logging of all signals during a test. The control is carried out on a real-  
 240 time NI controller (NI cRIO 9049), which shares the load signals so that both the test control and  
 241 logging system can access the load cell data.

### 242 3.1.3.1 Sensor

243 For this test campaign, the sensors used are described in Table 3, where the last three columns  
 244 refer to the sensors mounted on the blade, the sensors on the FastBlade system, and the number of  
 245 sensors the facility can handle, respectively. Oximate

246 *Table 3. List of sensors used.*

Sensor	Measurement Range	Accuracy / Non-linearity	No. Blade	No. FastBlade	Capacity
Load cell	±500 kN	±0.05%	1	4	4
Load cell	±25 kN	±0.001% FS	0	1	1
Accelerometer	±10 G	<3% FS	0	4	4
Accelerometer	±6 G	<3% FS	10	0	10
Linear Position	0-1000mm	±0.02% FS	4	0	4
Strain Gauge Linear	Strain Limit 5%		6x350Ω	6x350Ω	44x350Ω
Strain Gauge Rosette	Strain Limit 3%		16x120Ω	0	16x120Ω
Thermocouple	-200 to 1260 °C		10	12	32
Linear String Potentiometer	2000 mm	±0.1%	2	0	2

247 *The sensor positions on the blade surface (see (a) Sensor locations on the top side of the blade.*  
 248 *(b) Coordinate system for blade loads.*

249 Figure 5 (a)) are described using a coordinate system which references lines projected onto the  
 250 blade surface. The longitudinal lines run between the centre of the root connection to the centre of  
 251 the lifting eye connection at the blade tip. The crosswise coordinates on the blade are defined as  
 252 projected lines wrapping around the blade at set distances away from and parallel to the root  
 253 connection. Crosswise, line 1 is located 900 mm from the root; all other lines after that are equally  
 254 spaced at 800 mm intervals **towards the blade tip**. The sensor coordinates are defined using the  
 255 crosswise line they are on first, followed by the longitudinal line they are on.

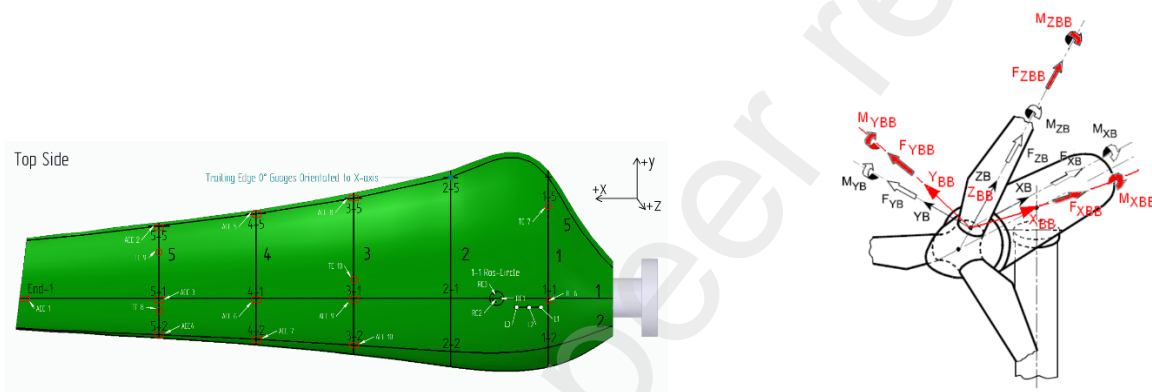
256 Moreover, the blade was monitored using Digital Image Correlation (DIC) equipment. Two sets  
 257 of stereo-pair cameras were used to capture different regions of the blade. The first set was  
 258 positioned approximately 4 m away from the blade using 12 mm lenses to capture the entire surface  
 259 of the blade between the root connection and the saddle. The second set of cameras was focused

260 on a much smaller blade area at the transition from the metal hub connection to full composite,  
261 approximately 800 mm from the root.

### 262 3.2 Set up

263 *The loading direction was based on the documentation available in the Extreme and Fatigue Load Calculations for Deepgen 500*  
264 *kW Tidal Turbine [27], which describes the axis systems for the blade (see (a) Sensor locations on the top side of the blade.*  
265 *(b) Coordinate system for blade loads.*

266 Figure 5 (a)). By combining the loading in the XB and YB directions, an actuator angle of  $14.58^\circ$   
267 anti-clockwise from the XB axis was identified as the optimal loading direction when viewed from  
268 the blade tip. Based on the static and fatigue loads, the optimal distance an actuator location of  
269 3.55m from the back face of the blade connection flange, pushing in the XBB direction, was  
270 identified as the loading location achieving the moment about the YBB axis.



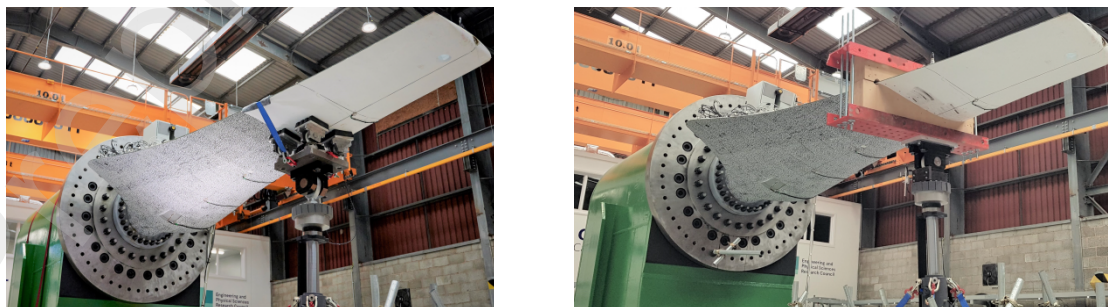
271  
272 (a) Sensor locations on the top side of the blade.

(b) Coordinate system for blade loads.

273 Figure 5. Sensor locations (left) and blade coordinate system (right).

274 *Two different methods were tested to apply the loads to the blade. Firstly, an articulated pad system was used (see (a)Articulated*  
275 *pad.*  
*(b) Clamping system.*

276 Figure 6 (a)). This system would not introduce additional bending moments to the specimen;  
277 nevertheless, some pad slippage was observed for over 100 mm in the Y direction towards the  
278 trailing edge. The second load introduction method was a clamped wooden saddle with a steel  
279 surrounding frame and a 1.5 mm thick silicone sheet at the blade interface. Even if the second  
280 system adds additional bending on the blade it would not be sufficient to affect the failure mode  
281 of a full-scale tidal blade.



282

283 (a) Articulated pad.

(b) Clamping system.

284 Figure 6. Load introduction system.

## 285 4. RESULTS

### 286 4.1 FastBlade's reaction frame performance

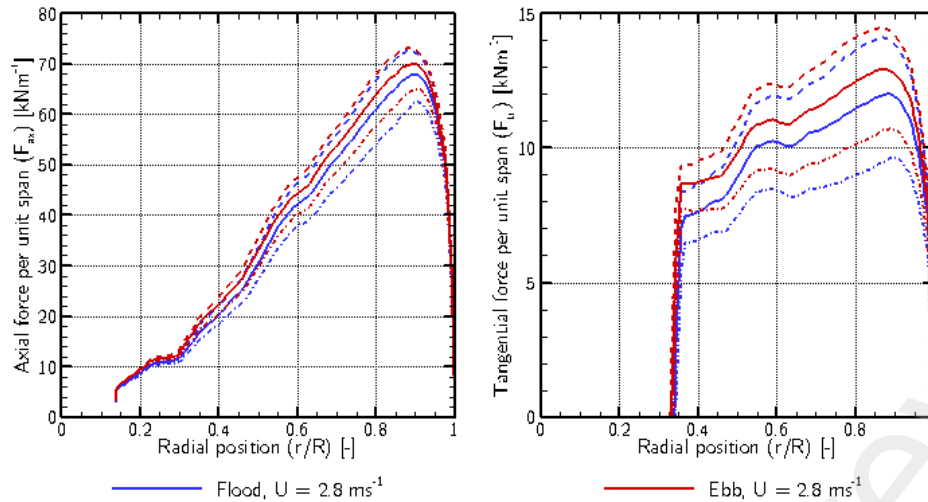
287 To quantify the stiffness of the reaction frame, a laser was used. The laser was mounted on the  
288 strong wall and pointed out to the far wall of the test hall. After applying a 200 kN load to the  
289 blade, the angle change of the strong wall was calculated to be  $0.00286^\circ$ . At this load, the tip  
290 deflection of the blade was 82 mm. The angle change of the strong wall contributed to 0.26 mm  
291 of this deflection (0.32%). This is below the 1% threshold, as stated in the PD IEC TS 62600-  
292 3:2020 A.9.4 [9], so it can be ignored.

### 293 4.2 Simulated blade loads

294 The rotor was simulated in flood and ebb tides across the range of flow speeds indicated in Table  
295 1. The turbine is designed to achieve rated power at a hub-height flow speed of  $2.8 \text{ ms}^{-1}$ , with a  
296 rotational speed of 13.78 rpm, implying an optimal tip speed ratio of  $\lambda = R\Omega/U = 4.64$ . This  
297 was maintained by adjusting the rotor speed for other upstream flow speeds. The rotor occupies a  
298 substantial proportion of the 43 m water depth at the site, and consequently, differences in rotor  
299 loads and performance were observed due to the different velocity shear profiles between the flood  
300 and ebb tides, even for the same hub-height velocity. Specifically, a slightly greater shear was  
301 observed across the rotor-swept area in the flood tide compared to the ebb tide.

302 The spanwise axial and tangential blade loads are shown in Figure 7, highlighting the mean,  
303 minimum and maximum loading profiles during a rotation. The minimum and maximum  
304 distributions have been selected based on the forces per unit span at the  $r/R=0.9$  location, which  
305 corresponds approximately to the location where the largest forces are encountered on the blade.  
306 Loads generally increase along the blade as a result of the increasing incident flow speed, driven  
307 by the rotational component of velocity. A negligible tangential force (contributing to rotor torque)  
308 is observed for  $r/R < 0.35$  due to the blending of the blade into the cylindrical root section in this  
309 region.

310 The sheared flow profile encountered by the rotor means that the mean blade loads are slightly  
311 higher for the rotor in the ebb tide than the flood tide due to two principal reasons. Firstly, the  
312 greater velocity shear across the rotor in the flood tide means that the mass flux through the rotor  
313 swept area is slightly lower than that for the ebb tide, for a given hub-height flow speed. This effect  
314 is more significant for higher flow speeds. Secondly, greater variation in flow speed through the  
315 rotor swept area results in the rotor operating further from its hydrodynamic optimum, which is  
316 seen as the increased minimum-maximum spread in blade loads. This has a greater impact on the  
317 blade in the lower part of the rotation due to the greater shear in this region, whereas the difference  
318 in velocity was less pronounced in the higher part of the water column.

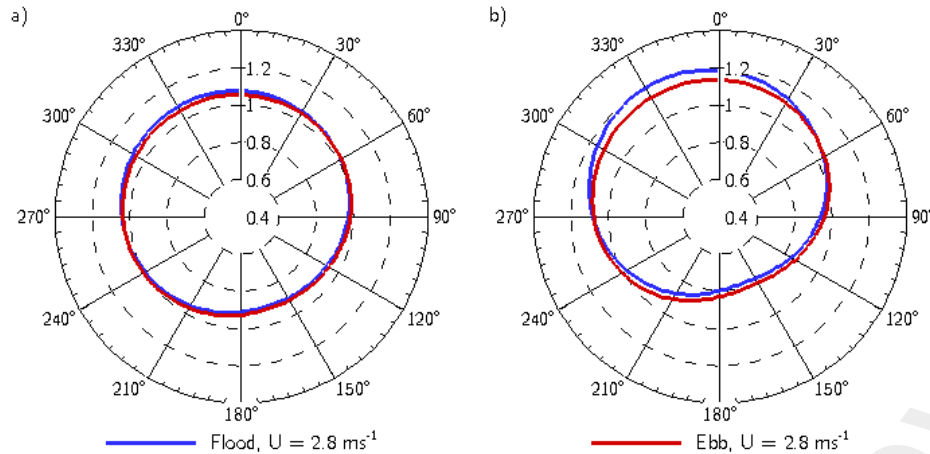


319

320 *Figure 7 Spanwise variation in axial (left) and tangential (right) force along a blade in the flood (blue) and ebb (red) tides at a*  
 321 *hub-height flow speed of  $2.8 \text{ ms}^{-1}$ . The mean load over a rotation is indicated with a solid line, with dashed and dash-dot lines*  
 322 *use.*

323 The simulations reproduced 1p and 3p fluctuations in blade loads and overall power and thrust as  
 324 a result of the rotational sampling of the shear profile by the blades, which also resulted in  
 325 azimuthal variations in blade root bending moments (RBM) shown in Figure 8. The results are  
 326 normalised on the respective means of the flood and ebb flapwise and edgewise RBMs in order to  
 327 highlight the azimuthal variations in loads. Normalised RBMs were generally higher for the rotor  
 328 operating in the ebb tide between  $90\text{-}270^\circ$  due to the reduced shear (higher flow speeds) in that  
 329 case, counterbalanced by the higher flood RBMs in the upper-half of the blade rotation.

330 While the magnitude of the flapwise RBMs was larger than that for the edgewise direction, the  
 331 relative variation in the edgewise RBMs was greater as a result of the greater sensitivity to the  
 332 angle of attack of the flow onto the blade. Additionally, the maximum and minimum RBMs were  
 333 not encountered at the top- and bottom- dead centre ( $0^\circ$  and  $180^\circ$ , respectively), but slightly offset  
 334 from these positions by about  $30^\circ$ . The rotor-induced swirl velocity interacts with the shear profile  
 335 to alter the flow incident on the rotor, and due to the different sensitivities of the flapwise and  
 336 edgewise directions to changes in the angle of attack, the minima and maxima occur at slightly  
 337 different azimuthal positions.



338

339 *Figure 8 Azimuthal variation in blade root bending moments in the flapwise (left) and edgewise (right) directions for the flood*  
 340 *(blue) and ebb (red) tides at a hub-height flow speed of  $U=2.8 \text{ ms}^{-1}$ . The bending moments have been normalised on their*  
 341 *respective mean.*

### 342 4.3 Blade Centre of Gravity

343 The centre of gravity is  $900 \pm 30$  mm from the blade's root. It is defined as the intersection of the  
 344 blade and a vertical line from the crane hook when the blade is aligned at  $90^\circ$  from that vertical  
 345 line. Simultaneously, the weight of the blade was obtained with an average value of 1588.59 kg  
 346 (15584.07 N).

### 347 4.4 Natural Frequency

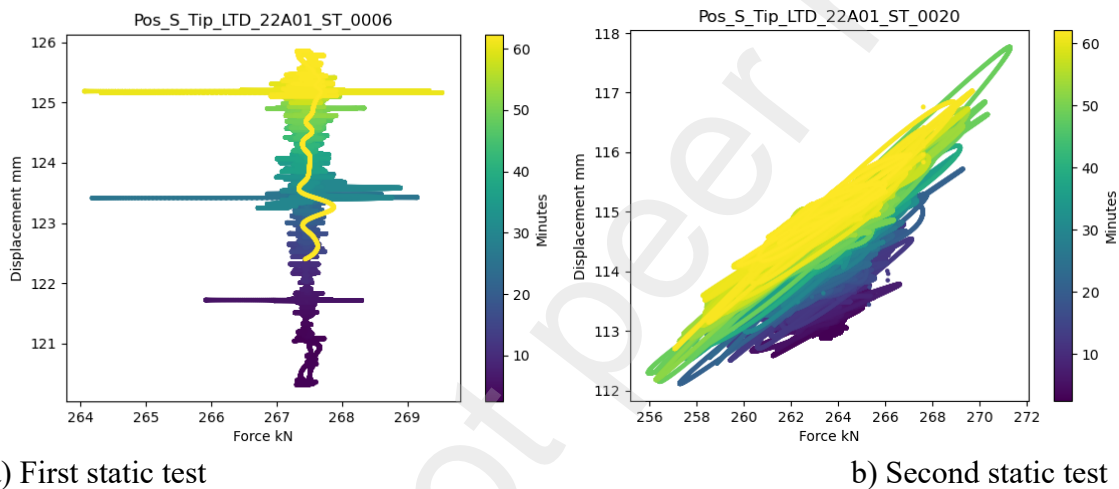
348 The natural frequency tests show a slight reduction from 18.0278 Hz before the test campaign  
 349 began to 17.9308 Hz at the end of the campaign. This reduction of 0.54% concerning the original  
 350 value suggests minor damage to the blade. Three measures were made on each natural frequency  
 351 test, and due to a change in the test process from moving to a clamp-on saddle, the post-fatigue  
 352 test was carried out with the saddle in place, so it is not comparable with the initial tests. A final  
 353 test at the end was carried out without the saddle attached to the blade to compare the initial tests.  
 354 These results are summarised in Table 4.

355 *Table 4. The result from Natural Frequency*

No Attached Test	Saddle	Natural Frequency (Hz)	Standard Deviation	Saddle Attached Test	Natural Frequency (Hz)	Standard Deviation
Pre-Campaign		18.0278	0.0057	Post Fatigue	14.8196	0.0053
Post-Static 1		18.0019	0.0035	Post-Static 2	14.7939	0.0021
Post-Campaign		17.9309	0.0026			

## 356 4.5 Static Loading

357 Two different static tests were performed, corresponding to tests three (first static test) and seven  
358 (second static test), for both cases; the target load was 273 kN, introduced in 120 seconds, sustained  
359 for 3600 seconds and unloaded in 120 seconds, following the guidance of the IEC 62600-3  
360 standard [9]. Figure 9 (a) shows that as the test progresses, the displacement of the blade's tip  
361 increases from 120.5 mm to almost 126 mm. This increase in displacement over time would  
362 typically indicate a decrease in stiffness from damage to the blade. However, due to the saddle  
363 slipping during the test, which altered the loading conditions, we cannot attribute the increase in  
364 displacement to damage in the blade. Figure 9 (b) shows the results of the tip displacement after  
365 the fatigue tests and using the clamping system, which produces a less stable load due to the  
366 increased stiffness of the loading saddle responding to the digital hydraulic system. Nevertheless,  
367 the blade tip displacement variation during the second static test was reduced to 2mm at the end  
368 of the test compared to a 5mm variation from the first static test.



369 a) First static test

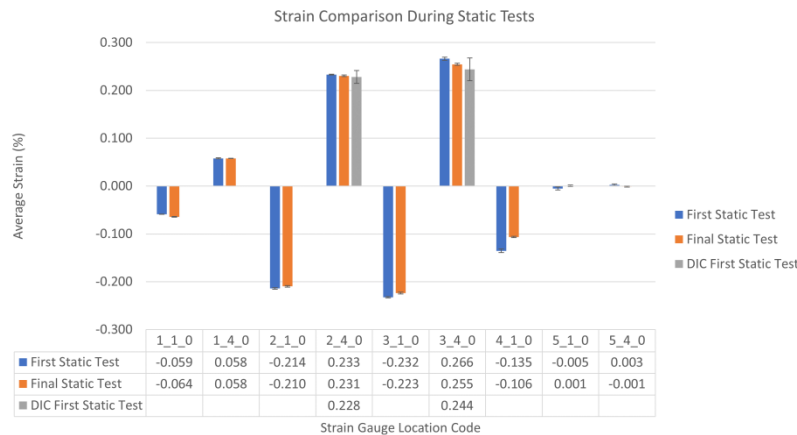
b) Second static test

371 *Figure 9. Blade tip displacement vs force over time.*

372 Damage has likely occurred between the tests, but the change in the saddle makes it challenging  
373 to be sure of the source of the observed variations. A comparison between the average strain in the  
374 initial and final static tests reveals that, in most cases, the strain values were reduced slightly, as  
375 seen in Figure 10. In the same figure, it can also be appreciated that the DIC strain captures the  
376 same trends in the strain as the rosette gauges, showing the same increases and drops along and  
377 strain values very similar to those measured by the gauges. Therefore, the DIC system can be



378 reliably used close to regions where where the data can be validated using the strain gauges.

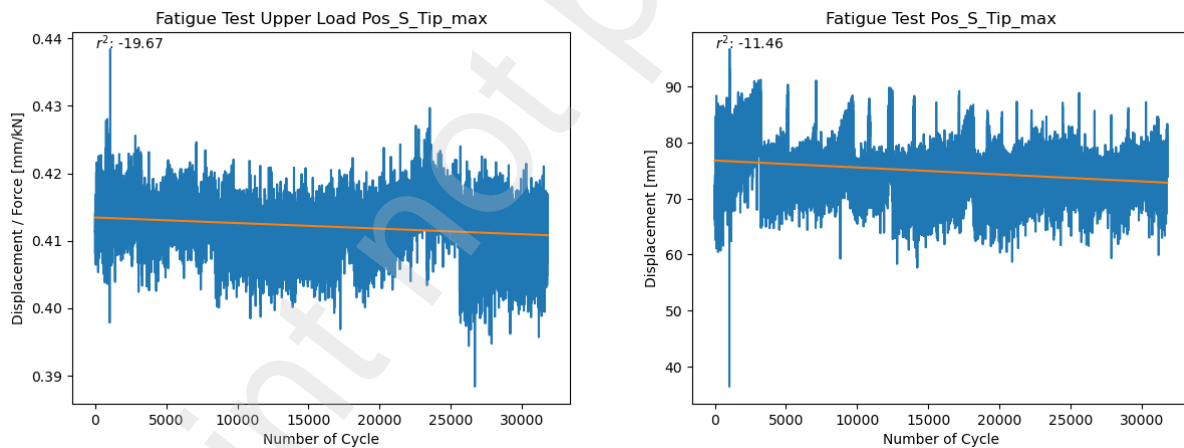


379

380 *Figure 10. Strain Comparison During Static Tests.*

### 381 4.6 Fatigue

382 Following the hydrodynamic results, the measured ocean data was extended to a year using  
 383 harmonic analysis; this allows us to define the most common bending moment at the root with a  
 384 magnitude of 652 kN-m. At the same actuator position as the static test, this gives a target load of  
 385 184 kN. During the fatigue test, 31,775 cycles were completed, equivalent to approximately 21.7  
 386 years of tidal cycles at 1 Hz.



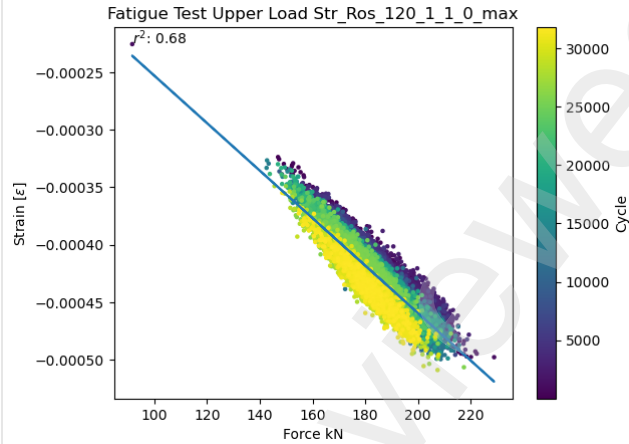
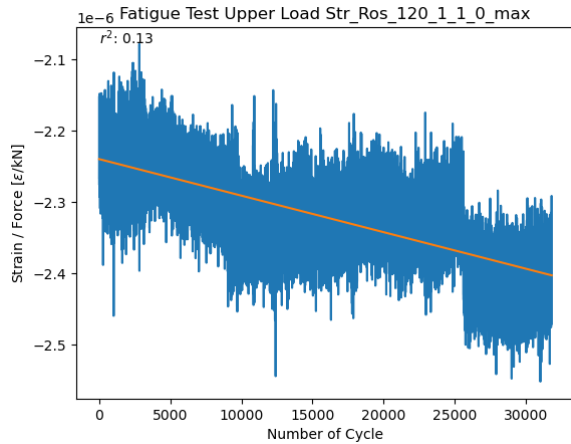
387

388 (a) *Blade tip Displacement/Force variations.*

388 (b) *Maximum tip displacement during the fatigue test.*

389 *Figure 11. Tip Displacement of Blades in Fatigue Loading.*

390 Figure 11 (a) presents the relationship between the tip displacement and force applied during the  
 391 test campaign. A slight downward trend can be observed, which might indicate an increase in blade  
 392 stiffness, but it is too subtle a change from which to draw any definitive conclusions. It is  
 393 interesting to see a significant drop between 20,000 and 25,000 cycles, which might indicate a  
 394 drastic change in stiffness. Additional testing and analysis will be required to draw any conclusion.  
 395 Figure 11 (b) shows that the maximum displacement reduces over time throughout the blade test.

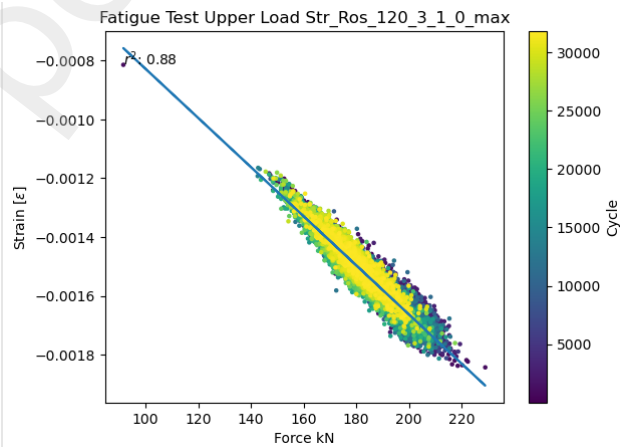
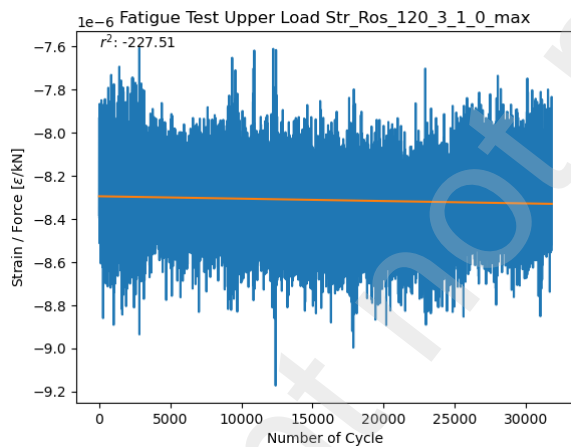


396  
397 (a) Strain/Force.

(b) Strain vs Load.

398 Figure 12. Strain behaviour during a fatigue test, blade top surface strain 900mm from the root.

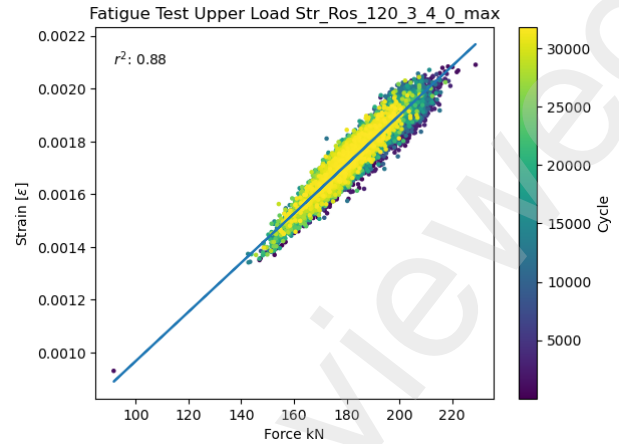
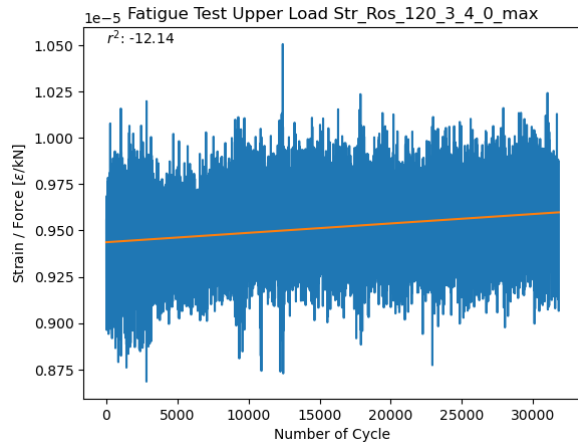
399 Figure 12 indicates that the magnitude of the strain in the blade increased (i.e. larger compression  
 400 strain) throughout the test at equivalent loads. This suggests that the blade at this location (1\_1\_0)  
 401 has reduced its stiffness. Figure 12 also indicates this with the downward trending line. Similar  
 402 behaviour is seen at locations 3\_1\_0 (see Figure 13) and 3\_4\_0 (see Figure 14). Moreover, it can  
 403 be appreciated that since these two strain gauges are in the exact location but one on the top and  
 404 one on the bottom of the blade, the results are almost a mirror of one to the other.



405  
406 (a) Strain/Force.

(b) Strain vs Load.

407 Figure 13. Strain behaviour during a fatigue test, blade top surface strain 2500mm from the root.



408

409 (a) Strain/Force.

(b) Strain vs Load.

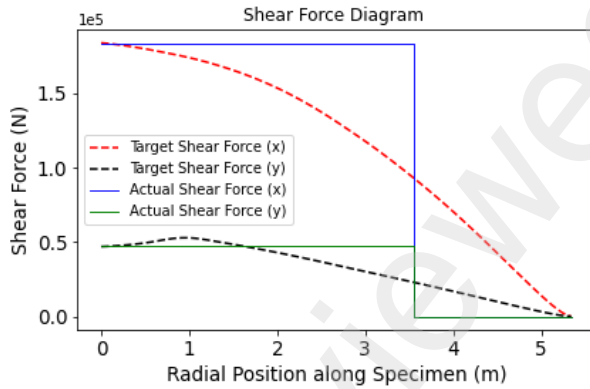
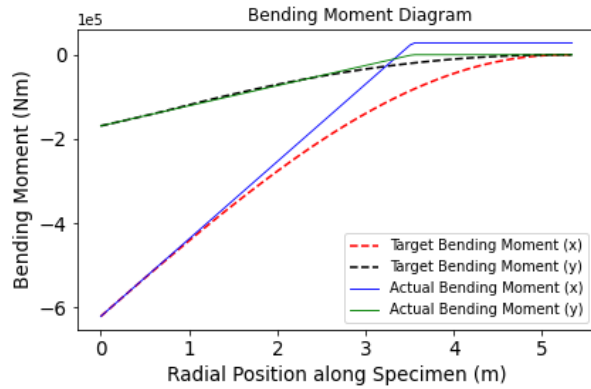
410 Figure 14. Strain behaviour during a fatigue test, blade bottom surface strain 2500mm from the root.

#### 411 4.7 Test evaluation

412 Overall the test is considered successful, nevertheless, during the initial static test the saddle  
 413 experienced some movement. This resulted in the load not being applied to the same location  
 414 throughout the test. This was solved by changing from a pad to a clamping system. It was seen  
 415 during the fatigue test that the PID control system struggles during a couple of cycles since tuning  
 416 is required during the test under changing conditions (i.e., change in the properties of the  
 417 specimen). This resulted in load cycles which either overshoot or undershoot target loads during  
 418 tuning.

419 The temperature of the test hall also varied by up to 10°C throughout testing. Where possible, this  
 420 was considered during the calibration procedures for the strain gauges and other sensors, but the  
 421 temperature variation during extended test periods could not be accounted for since it implies  
 422 multiple pauses during the test.

423 The load to be replicated for this test campaign is based on the data from the manufacturing  
 424 company for the static test and the hydrodynamic simulations. The shear stress and bending  
 425 moments were estimated for different flow conditions for the fatigue test. Since the test was  
 426 performed with one single actuator, it is evident that there will be limitations to achieving the same  
 427 spanwise forces and moments distribution. As mentioned in the set-up section, the position in  
 428 which the load is applied was chosen to minimise the difference between the used and calculated  
 429 loads; the comparison of the same can be seen in Figure 15.

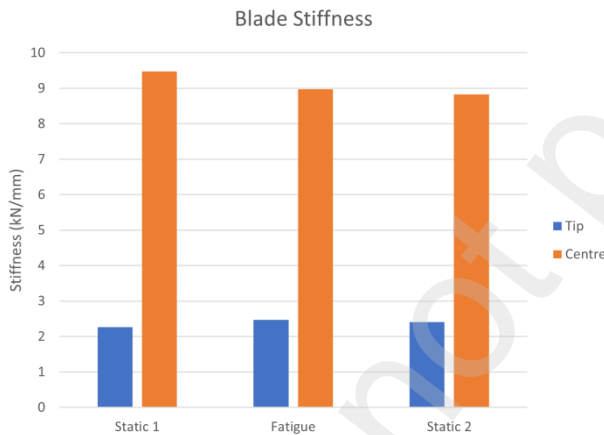


430  
431 (a) Bending moment.

(b) Shear Force.

432 Figure 15. Applied load evaluation.

433 Finally, the stiffness variation of the blade during the all-test campaign changes slightly, as seen  
 434 in Figure 16. The most notable changes seem to be at the tip; nevertheless, as mentioned, the result  
 435 from the first static test may not be completely accurate; overall, the stiffness changes seem to be  
 436 minimal, as shown in Table 5.



437  
438 Figure 16. Blade stiffness variations during the test campaign at the centre and tip.

439 Table 5. Blade's stiffness variation during the test campaign.

Test	Position	Displacement (mm)	Load (kN)	Stiffness (kN/mm)
Static 1	Tip	120.2	273	2.26
Fatigue	Tip	68.67	169.64	2.47
Static 2	Tip	114.53	276	2.41
Static 1	Centre	28.8	273	9.47
Fatigue	Centre	18.91	170	8.97
Static 2	Centre	31.24	276	8.83

440

## 5. CONCLUSIONS AND FUTURE WORK

441 This paper demonstrates that the FastBlade fatigue test facility can successfully perform a  
442 complete tidal blade mechanical fatigue test, following the available standards. This test campaign  
443 allowed the FastBlade team to identify several testing procedure improvements, i.e., control  
444 strategies, load introduction, instrumentation layout, instrument calibration, and test design.  
445 Finally, the facility opens a series of possibilities to tidal energy developers, designers and  
446 researchers due to FastBlade capacity to collect large amounts of data under controlled conditions  
447 while replicating many different load scenarios in a fast and economical way.

448 The blade tested survived the worst-case static load criteria defined by the developer. Moreover,  
449 the blade withstood 20 years (equivalent) of accelerated fatigue loading without catastrophic  
450 failure. No specific failures were observed throughout all testing. No audible sounds of failure  
451 were detected, nor sudden changes in position or load. The DIC system did not detect any areas of  
452 exceptionally raised strain. The highest strain measured with strain gauges was 0.266% on the  
453 bottom surface of the blade, near the loading saddle. All this suggests an overdesign on the blade,  
454 considering that the blade was under the ocean in working conditions for a few years before the  
455 test campaign.

456 A numerical model of the tested blade will be developed and calibrated using the data of the current  
457 experiment campaign. A new test campaign will be carried out in the future, in which a 3-actuator  
458 system will be used; this will allow having a more complex load introduced into the blade and  
459 compare the results to a more traditional one-actuator system. In a new test campaign, the effect  
460 of the saddle clamped to the system will be tracked to detect any possible induced shear stress  
461 previous to the test. More sensors will be added to the blade and the FastBlade system (i.e.,  
462 microphones) to capture more information and evaluate machine learning algorithms to detect any  
463 anomaly behaviour.

464

## 6. ACKNOWLEDGEMENTS

465 First Author: This project has received funding from the European Union's Horizon 2020 research  
466 and innovation programme under the Marie Skłodowska-Curie grant agreement No 801215 and  
467 the University of Edinburgh Data-Driven Innovation programme, part of the Edinburgh and South  
468 East Scotland City Region Deal.

469 All authors: The authors also wish to thank the Supergen ORE Hub for funding received through  
470 the Flexible Fund Award FF2020-1063.

471

## 7. REFERENCES

472 [1] H. Jeffrey, S. Pennock, JLVillate, P Ruiz-Minguela, D. Cagney, L. Pirttimaa, A European  
473 Ocean Energy Industry – the €140bn Economic Opportunity, Industrial Roadmap for  
474 Ocean Energy, (n.d.). [https://www.etipocean.eu/knowledge\\_hub/industrial-roadmap-for-](https://www.etipocean.eu/knowledge_hub/industrial-roadmap-for-ocean-energy/)  
475 [ocean-energy/](https://www.etipocean.eu/knowledge_hub/industrial-roadmap-for-ocean-energy/) (accessed January 13, 2023).

476 [2] European Commission, Tidal flows generate huge potential for clean electricity | Research  
477 and Innovation, (n.d.). <https://ec.europa.eu/research-and-innovation/en/projects/success->

- 478 stories/all/tidal-flows-generate-huge-potential-clean-electricity (accessed January 13,  
479 2023).
- 480 [3] D.M. Grogan, S.B. Leen, C.R. Kennedy, C.M. Ó Brádaigh, Design of composite tidal  
481 turbine blades, *Renew. Energy*. 57 (2013) 151–162.  
482 <https://doi.org/10.1016/j.renene.2013.01.021>.
- 483 [4] C.R. Kennedy, S.B. Leen, C.M. M.M. Brádaigh, A preliminary design methodology for  
484 fatigue life prediction of polymer composites for tidal turbine blades, *Proc. Inst. Mech.*  
485 *Eng. Part L J. Mater. Des. Appl.* 226 (2012) 203–218.  
486 <https://doi.org/10.1177/1464420712443330>.
- 487 [5] C.R. Kennedy, V. Jaksic, S.B. Leen, C.M. Ó. Brádaigh, Fatigue life of pitch- and stall-  
488 regulated composite tidal turbine blades, *Renew. Energy*. 121 (2018) 688–699.  
489 <https://doi.org/10.1016/j.renene.2018.01.085>.
- 490 [6] W. Li, H. Zhou, H. Liu, Y. Lin, Q. Xu, Review on the blade design technologies of tidal  
491 current turbine, *Renew. Sustain. Energy Rev.* 63 (2016) 414–422.  
492 <https://doi.org/10.1016/j.rser.2016.05.017>.
- 493 [7] A. S. Evans, Analysis: Record-low price for UK offshore wind is nine times cheaper than  
494 gas - Carbon Brief, (n.d.). [https://www.carbonbrief.org/analysis-record-low-price-for-uk-](https://www.carbonbrief.org/analysis-record-low-price-for-uk-offshore-wind-is-four-times-cheaper-than-gas/)  
495 [offshore-wind-is-four-times-cheaper-than-gas/](https://www.carbonbrief.org/analysis-record-low-price-for-uk-offshore-wind-is-four-times-cheaper-than-gas/) (accessed January 13, 2023).
- 496 [8] O. de la Torre, D. Moore, D. Gavigan, J. Goggins, Accelerated life testing study of a novel  
497 tidal turbine blade attachment, *Int. J. Fatigue*. 114 (2018) 226–237.  
498 <https://doi.org/10.1016/J.IJFATIGUE.2018.05.029>.
- 499 [9] British Standards Institution, Marine energy. Wave, tidal and other water current  
500 converters. Part 3, Measurement of mechanical loads., British Standards Institution, 2020.  
501 <https://www.document-center.com/standards/show/PD-IEC-62600-3> (accessed January  
502 13, 2023).
- 503 [10] F.R. Cuthill, J.R. Steynor, S.L. Dubon, E.D. Mccarthy, C. Conch', C.M.' Brádaigh, J.R.  
504 Steynor Is Senior, E.D. Mccarthy, Development of the world's first regenerative hydraulic  
505 tidal blade test centre: FASTBLADE, in: *Eur. Wave Tidal Energy Conf. 14th EWTEC*,  
506 Plymouth, 2021. <https://proceedings.ewtec.org/product/ewtec-2021-plymouth-uk/>  
507 (accessed January 13, 2023).
- 508 [11] C. Glennon, W. Finnegan, N. Kaufmann, · Patrick Meier, Y. Jiang, R. Starzmann, J.  
509 Goggins, Tidal stream to mainstream: mechanical testing of composite tidal stream blades  
510 to de-risk operational design life, *J. Ocean Eng. Mar. Energy*. 8 (2022) 163–182.  
511 <https://doi.org/10.1007/s40722-022-00223-4>.
- 512 [12] N. Caldwell, Review of early work on digital displacement® hydrostatic transmission  
513 systems, BATH/ASME 2018 Symp. Fluid Power Motion Control. FPMC 2018. (2018).  
514 <https://doi.org/10.1115/FPMC2018-8922>.
- 515 [13] M. Ehsan, W.H.S. Rampen, S.H. Salter, Modeling of digital-displacement pump-motors  
516 and their application as hydraulic drives for nonuniform loads, *J. Dyn. Syst. Meas.*  
517 *Control. Trans. ASME*. 122 (2000) 210–215. <https://doi.org/10.1115/1.482444>.
- 518 [14] W. Rampen, D. Dumnov, J. Taylor, H. Dodson, J. Hutcheson, N. Caldwell, A Digital

- 519 Displacement Hydrostatic Wind-turbine Transmission, *Int. J. Fluid Power*. 21 (2021) 87–  
520 112–87–112. <https://doi.org/10.13052/IJFP1439-9776.2213>.
- 521 [15] B. Sellar, Metocean Data Set from the ReDAPT Tidal Project: Batch 1, Part 2, 2011-2014,  
522 (2017). <https://doi.org/https://doi.org/10.7488/ds/1687>.
- 523 [16] B.G. Sellar, TIDAL ENERGY SITE CHARACTERISATION AT THE FALL OF  
524 WARNESS, EMEC, UK, Edinburgh, 2016.  
525 [https://redapt.eng.ed.ac.uk/library/eti/reports\\_updated/Technical Report on Tidal Site  
526 Characaterisation During the ReDAPT Project v4.0.pdf](https://redapt.eng.ed.ac.uk/library/eti/reports_updated/Technical%20Report%20on%20Tidal%20Site%20Characaterisation%20During%20the%20ReDAPT%20Project%20v4.0.pdf).
- 527 [17] B.G. Sellar, G. Wakelam, D.R.J. Sutherland, D.M.I. Id, V. Venugopal, Characterisation of  
528 Tidal Flows at the European Marine Energy Centre in the Absence of Ocean Waves,  
529 *Energies*. 11 (2018). <https://doi.org/10.3390/en11010176>.
- 530 [18] U. Ahmed, D.D. Apsley, I. Afgan, T. Stallard, P.K. Stansby, Fluctuating loads on a tidal  
531 turbine due to velocity shear and turbulence: Comparison of CFD with field data, *Renew.  
532 Energy*. 112 (2017) 235–246. <https://doi.org/10.1016/J.RENENE.2017.05.048>.
- 533 [19] F.R. Menter, M. Kuntz, R. Langtry, Ten Years of Industrial Experience with the SST  
534 Turbulence Model, *Turbul. Heat Mass Transf.* 4. (2003).  
535 <http://aaac.larc.nasa.gov/tsab/cfdlarc/aiaa-dpw/> (accessed January 13, 2023).
- 536 [20] J.N. Sørensen, W.Z. Shen, Numerical Modeling of Wind Turbine Wakes, *J. Fluids Eng.*  
537 124 (2002) 393–399. <https://doi.org/10.1115/1.1471361>.
- 538 [21] J. Schluntz, R.H.J.J. Willden, An actuator line method with novel blade flow field  
539 coupling based on potential flow equivalence, *Wind Energy*. 18 (2015) 1469–1485.  
540 <https://doi.org/10.1002/we.1770>.
- 541 [22] A. Wimshurst, R.H.J. Willden, Analysis of a tip correction factor for horizontal axis  
542 turbines, *Wind Energy*. 20 (2017) 1515–1528. <https://doi.org/10.1002/WE.2106>.
- 543 [23] W.Z. Shen, J.N. Sørensen, R. Mikkelsen, Tip Loss Correction for Actuator/Navier–Stokes  
544 Computations, *J. Sol. Energy Eng.* 127 (2005) 209–213.  
545 <https://doi.org/10.1115/1.1850488>.
- 546 [24] D.D. Apsley, T. Stallard, P.K. Stansby, Actuator-line CFD modelling of tidal-stream  
547 turbines in arrays, *J. Ocean Eng. Mar. Energy*. 4 (2018) 259–271.  
548 <https://doi.org/10.1007/S40722-018-0120-3/FIGURES/17>.
- 549 [25] C. L. Larson, C.W. Brooks, A.S.H. Jr, D.W. Sproles., Computer program to obtain  
550 ordinates for NACA airfoils. Tech Report 4741, Hampton, Virginia, USA, 1996.  
551 <https://ntrs.nasa.gov/api/citations/19970008124/downloads/19970008124.pdf>.
- 552 [26] C. Huxley-Reynard, J. Thake, G. Gibberd, TG-RE-040-0091 Rev B Deepgen Blade  
553 Design Report, Bristol, 2008.
- 554 [27] C. Huxley-Reynard, J. King, G. Gibberd, TG-RE-000-0081 Rev D Extreme and Fatigue  
555 Load Calculations for Deepgen 500kW Tidal Turbine, Bristol, 2008.
- 556